Hindawi
Mathematical Problems in Engineering
Volume 2019, Article ID 6384132, 15 pages
https://doi.org/10.1155/2019/6384132

Research Article

A New Iterative Algorithm Based on Correction of Sensitivity Matrix for Electrical Resistance Tomography

Yutong Chen,[1,2] **Yan Han**,[1] **Wuqiang Yang**,[3] **and Kun Li**[1,4]

[1]*Shanxi Key Lab of Signal Capturing and Processing, North University of China, Taiyuan 030051, China*
[2]*Department of Electrical Engineering and Automation, Shanxi Polytechnic College, Taiyuan 030006, China*
[3]*Department of Electrical and Electronic Engineering, University of Manchester, Manchester M13 9PL, UK*
[4]*School of Chemical and Process Engineering, University of Leeds, Leeds LS2 9JT, UK*

Correspondence should be addressed to Yutong Chen; cyt_nuc@163.com

Received 25 June 2019; Revised 16 August 2019; Accepted 21 August 2019; Published 28 December 2019

Academic Editor: Elisa Francomano

Electrical resistance tomography (ERT) is used to reconstruct the resistance/conductivity distribution. Usually, a uniform distribution is assumed as the initial condition to obtain a generic sensitivity matrix, which may be very different from a theoretical sensitivity matrix, resulting in a large error. The aim of this study is to analyse the difference between a generalized sensitivity matrix and a theoretical sensitivity matrix and to improve image reconstruction. The effect of the generic sensitivity matrix and theoretical sensitivity matrix on image reconstruction is analyzed. The error caused by the use of the generic sensitivity matrix is estimated. To reduce the error, an improved iterative image reconstruction algorithm is proposed, which is based on calculation of the error between the generic sensitivity matrix and the theoretical sensitivity matrix, and a correction coefficient with a penalty. During the iterative process, the resistivity distribution and sensitivity matrix are alternatively corrected. Simulation and experimental results show that the proposed algorithm can improve the quality of images, e.g., of two-phase distributions.

1. Introduction

As a fast, nonradiation, nonintrusive, and low-cost imaging technique, electrical resistance tomography (ERT) [1] has been developed for visualizing the internal conductivity distribution of industrial processes, by providing 2D/3D images. ERT has been widely used for chemical [2], food processing [3], biology [4], geology [5], and other industrial applications [6]. In ERT, usually a current is injected to a pair of electrodes and the boundary voltages are measured from other pairs of electrodes [7]. A particular difficulty for ERT is that its "soft field" [8] makes the inverse problem be nonlinear and ill posed, and hence the spatial resolution is limited. Various image reconstruction algorithms have been developed for ERT, such as linear back-projection (LBP) [9], Landweber iteration [10], and Tikhonov regularization [11]. Usually, a uniform distribution is assumed as the initial condition to obtain a generic sensitivity matrix.

Recently, several modified algorithms have been proposed. For example, Zhang [12] and Xiao et al. [13], respectively, used the results obtained by Landweber iteration and Newton–Raphson algorithms as the initial condition for updating a sensitivity matrix. These modified algorithms can reduce the reconstruction error caused by a generic sensitivity matrix and improve the image quality.

In this paper, the effect of the generic sensitivity matrix on image quality is analyzed, and a new image reconstruction algorithm is proposed, which is based on calculating the error introduced by the generic sensitivity matrix according to the variation in the boundary voltage. This algorithm includes a penalty factor, which can correct the sensitivity matrix during the iterative image reconstruction process.

2. Principle of ERT

2.1. Mathematical Model. An ERT sensor is shown in Figure 1 [14]. It shows that a current is injected into a pair of adjacent electrodes and the voltages between the remaining pairs of adjacent electrodes are measured. The injection and measurement are sequentially conducted until each adjacent electrode pair is used for current injection. For a 16-electrode ERT sensor, 104 independent measurements can be obtained.

When a perturbation $\Delta\boldsymbol{\sigma} \ll \boldsymbol{\sigma}_0$ (uniform conductivity) is small, according to the sensitivity coefficient principle, a linearised model for current injection and voltage measurement (see Figure 1) is given by [15]

$$\mathbf{S} \cdot \Delta\boldsymbol{\sigma} = \Delta\mathbf{Z}, \tag{1}$$

where $\Delta\mathbf{Z} = [\Delta\mathbf{Z}_1, \Delta\mathbf{Z}_1, \ldots, \Delta\mathbf{Z}_{M_Z}]^T$ is a $M_Z \times 1$ vector of change in measured boundary voltage, $\Delta\boldsymbol{\sigma} = [\Delta\boldsymbol{\sigma}_1, \Delta\boldsymbol{\sigma}_2, \ldots, \Delta\boldsymbol{\sigma}_{M_\sigma}]^T$ is a $M_\sigma \times 1$ vector of change in conductivity, and $\mathbf{S} = [S_{ij}]_{M_Z \times M_\sigma}$ is a calculated sensitivity matrix, where S_{ij} is the sensitivity coefficient of the jth pixel relative to the ith measurement.

Once the change in boundary voltage $\Delta\mathbf{Z}$ and the sensitivity matrix $\mathbf{S}$ have been obtained, a vector of change in conductivity $\Delta\boldsymbol{\sigma}$ can be calculated, e.g., using Landweber iteration algorithm [10]

$$\begin{cases} \Delta\boldsymbol{\sigma}_{k+1} = \Delta\boldsymbol{\sigma}_k + \alpha \cdot \mathbf{S}^T (\Delta\mathbf{Z} - \mathbf{S} \cdot \Delta\boldsymbol{\sigma}_k), \\ \Delta\boldsymbol{\sigma}_1 = \mathbf{S}^T \Delta\mathbf{Z}, \end{cases} \tag{2}$$

where $\Delta\boldsymbol{\sigma}_k$ is a vector of change in conductivity at the kth iteration and α is the step length.

From $\Delta\boldsymbol{\sigma}$, the conductivity distribution vector $\boldsymbol{\sigma}$ can be obtained by

$$\boldsymbol{\sigma} = Q[\boldsymbol{\sigma}_0 + \Delta\boldsymbol{\sigma}], \tag{3}$$

where $Q[\,]$ is the projection operator [16], so that the conductivity distribution is limited between 0 and 1.

2.2. Effect of Sensitivity Matrix on Image Reconstruction. In equation (2), the sensitivity matrix $\mathbf{S}$ changes with the conductivity distribution $\boldsymbol{\sigma}$, causing serious ill posedness and nonlinearity, as shown in Figure 2. $\boldsymbol{\sigma}$ can be solved by $F(\boldsymbol{\sigma}) = \mathbf{Z}$ [17], where $\mathbf{Z}$ is the boundary voltage vector. It is common that the sensitivity matrix is used to estimate the boundary voltage based on the conductivity distribution, which is called forward projection:

$$\mathbf{S}\boldsymbol{\sigma} = \mathbf{Z}. \tag{4}$$

In practice, the sensitivity matrix $\mathbf{S}$ cannot be used to solve the problem because $\mathbf{S}$ changes with the conductivity distribution $\boldsymbol{\sigma}$. Therefore, only the uniform field sensitivity matrix $\mathbf{S}_0$ can be used to find the approximate solution to the conductivity distribution by equation (1). Figure 3 shows a reconstructed image using a theoretical sensitivity matrix and another image using a generic sensitivity matrix based on a uniform field distribution.

Comparing Figure 3(a) with 3(b), it can be seen that the area of discrete-phase is enlarged and the edge of two phases is not distinct with artifacts near the boundary, i.e., the image is significantly degraded. The main reason for this is that the sensitivity matrix in equation (1) is only suitable for the case, where the additional perturbation $\Delta\boldsymbol{\sigma}$ of the sensing field is small [17] and the error is larger with a larger $\Delta\boldsymbol{\sigma}$.

3. Error Penalty Reconstruction Based on Landweber Iteration

3.1. Error Introduced by Generic Sensitivity Matrix. Assuming that the theoretical sensitivity matrix $\mathbf{S}$ is known, the following equation can be obtained from equation (4):

$$\mathbf{S} \cdot \boldsymbol{\sigma} - \mathbf{S}_0 \cdot \boldsymbol{\sigma}_0 = \mathbf{Z} - \mathbf{Z}_0, \tag{5}$$

where $\mathbf{Z}_0$ is the boundary voltage vector of uniform field $\boldsymbol{\sigma}_0$.

Because $\mathbf{S}$ cannot be obtained when $\boldsymbol{\sigma}$ is unknown, the inverse problem is usually solved by equation (1) using a generic sensitivity matrix $\mathbf{S}_0$. Equation (1) can be rewritten as

$$\mathbf{S}_0 \cdot \Delta\boldsymbol{\sigma} = \Delta\mathbf{Z}, \tag{6}$$

where $\Delta\mathbf{Z} = \mathrm{Z} - \mathrm{Z}_0$. Then, equation (6) can be expanded to

$$\mathbf{S}_0\boldsymbol{\sigma} - \mathbf{S}_0\boldsymbol{\sigma}_0 = \mathbf{Z} - \mathbf{Z}_0. \tag{7}$$

Comparing with equation (5), the theoretical sensitivity matrix $\mathbf{S}$ is replaced by the generic sensitivity matrix $\mathbf{S}_0$. To analyse the error, equation (7) is rewritten as

$$\mathbf{S}\boldsymbol{\sigma} - \mathbf{S}_0\boldsymbol{\sigma}_0 + (\mathbf{S}_0 - \mathbf{S})\boldsymbol{\sigma} = \mathbf{Z} - \mathbf{Z}_0, \tag{8}$$

and hence

$$\boldsymbol{\eta} = (\mathbf{S}_0 - \mathbf{S})\boldsymbol{\sigma}. \tag{9}$$

It is the error vector introduced when the theoretical sensitivity matrix is replaced. For simplicity, $\boldsymbol{\eta}$ is called "matrix substitution error" in this paper, which can be ignored when $\Delta\boldsymbol{\sigma} = (\boldsymbol{\sigma} - \boldsymbol{\sigma}_0)$ is small. However, when the conductivity distribution changes significantly compared with the uniform field, $\boldsymbol{\eta}$ also becomes larger and would result in a larger reconstruction error.

If the conductivity distribution $\widetilde{\sigma}$ can be found, which is close enough to the real distribution $\boldsymbol{\sigma}$ as the initial distribution, and its corresponding sensitivity matrix $\widetilde{S}$ can be used as the initial sensitivity matrix, then

$$\widetilde{S}\boldsymbol{\sigma} - \widetilde{S}\widetilde{\sigma} = \mathbf{Z} - \widetilde{Z}. \tag{10}$$

As a result, the error $\boldsymbol{\eta} = (\widetilde{S} - \mathbf{S})\boldsymbol{\sigma}$ can be effectively reduced, improving the image quality.

3.2. Sensitivity Matrix Correction with Penalty Factor. Considering Landweber's solution as the initial distribution $\widetilde{\sigma}$ in equation (10), the distribution is obtained by the generic sensitivity matrix and the size of the error $\boldsymbol{\eta}$ is different from each other for different distribution. To reduce the error, the change in distribution calculated by conventional Landweber iterative algorithm needs to be constrained differently according to the distribution. In equation (9), it can be seen

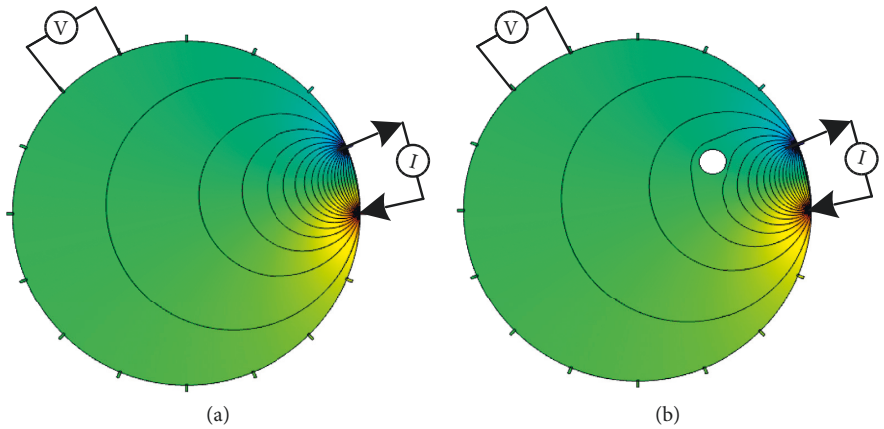

Figure 1: 16-electrode ERT sensor model. (a) Uniform conductivity. (b) Perturbed conductivity.

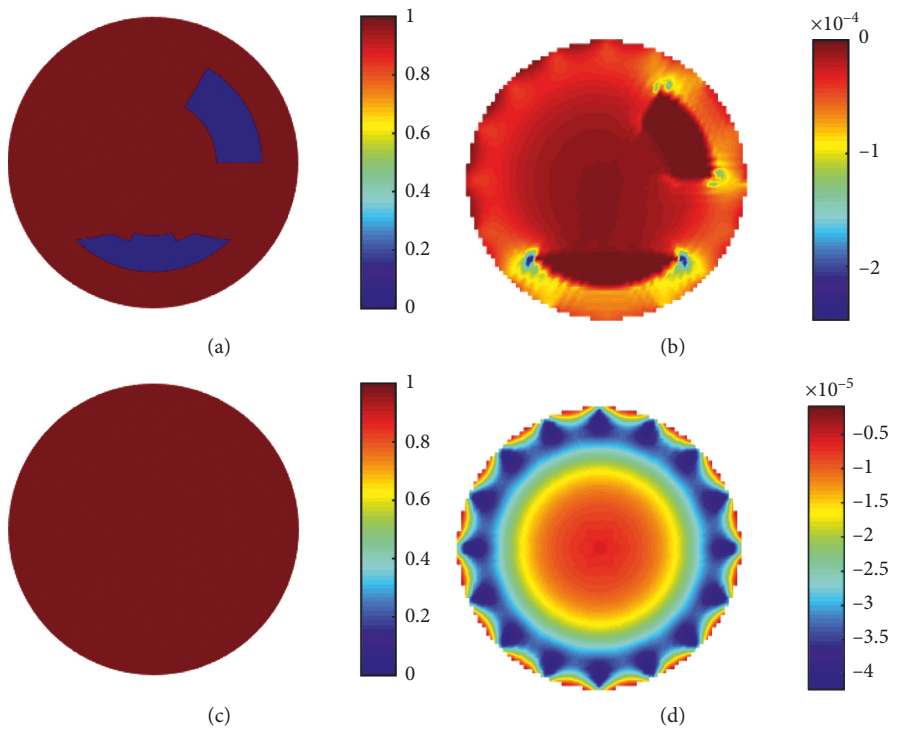

Figure 2: Different conductivity distributions and corresponding sensitivity matrix. (a) Conductivity distribution of D1. (b) Mean of sensitivity matrix of D1. (c) Uniform distribution. (d) Mean of sensitivity matrix of uniform distribution.

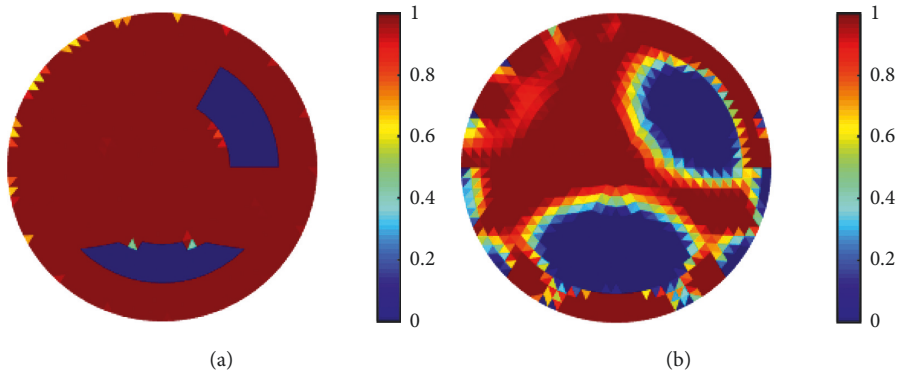

Figure 3: Reconstructed image of model D1. (a) Using theoretical sensitivity matrix of D1. (b) Using sensitivity matrix of uniform field.

that if the difference between the generic sensitivity matrix $\mathbf{S}_0$ and the theoretical sensitivity matrix $\mathbf{S}$ is small, the error $\boldsymbol{\eta}$ is small and the reconstruction result $\Delta\widetilde{\sigma}$ is accurate. The greater difference between them would result in the larger error of reconstruction. Therefore, a penalty factor μ associated with $\boldsymbol{\eta}$ is chosen to penalize the error of $\Delta\widetilde{\sigma}$. However, the theoretical error $\boldsymbol{\eta}$ cannot be obtained when the true distribution $\boldsymbol{\sigma}$ is unknown. Therefore, it is necessary to use other related known quantities to determine the penalty factor μ.

In equation (4), the measured boundary voltage vector $\mathbf{Z}$ is related to the theoretical sensitivity matrix $\mathbf{S}$ and the true distribution $\boldsymbol{\sigma}$. Therefore, a method is proposed to estimate the error $\boldsymbol{\eta}$ using the change in boundary voltage $\Delta\mathbf{Z}$. The relative changes in the boundary voltage is

$$\mu = \frac{|\Delta\mathbf{Z}|}{|\mathbf{Z}_0|}. \tag{11}$$

It is set as the penalty factor. From equations (5) and (9), it can be seen that μ would increase as $\boldsymbol{\eta}$ increases. A correction coefficient is defined as

$$\beta = B - \mu. \tag{12}$$

It is used to correct $\Delta\widetilde{\sigma}$ obtained by Landweber algorithm, where B is a constant. Considering the convergence rate and stability, B can be selected between 0.5 and 1.5. Then, equation (3) can be rewritten as

$$\widetilde{\sigma} = Q\left[\boldsymbol{\sigma}_0 + \beta \cdot \Delta\widetilde{\sigma}\right]. \tag{13}$$

After the conductivity distribution is corrected, a corrected sensitivity matrix $\widetilde{S}$ can be obtained. Then, the corrected distribution $\widetilde{\sigma}$ and sensitivity matrix $\widetilde{S}$ can be used as the initial value in equation (10), to further reduce the image error.

3.3. Improved Landweber Algorithm. The following is about approximating the true field distribution by multiple corrections. During this process, the error changes as

$$\boldsymbol{\eta}_p = \mathbf{S}_p - \mathbf{S}, \tag{14}$$

where $p = 0, 1, \ldots, P$ is the correction time, $\mathbf{S}_p$ is the sensitivity matrix corresponding to the pth distribution corrected. When $p = 0$, the initial value is corresponding to the uniform field.

The correction factor for the $p+1$st correction is adjusted as

$$\beta_{p+1} = B - \mu_{p+1}, \tag{15}$$

where $\mu_{p+1} = |\Delta\mathbf{Z}_p|/|\mathbf{Z}_p|$ and $\Delta\mathbf{Z}_p = \mathbf{Z} - \mathbf{Z}_p$, $\mathbf{Z}_p$ is the calculated boundary voltage corresponding to $\boldsymbol{\sigma}_p$ after the pth correction. Because μ_{p+1} is related to the error $\boldsymbol{\eta}_p$, with the approximation, whether or not further correction of the sensitivity matrix is needed can be determined by μ_{p+1}:

$$\mu_{p+1}\begin{cases} <\varepsilon, & \text{No need to correct the sensitivity matrix,} \\ \geq\varepsilon, & \text{Need to correct the sensitivity matrix.} \end{cases} \tag{16}$$

The improved reconstruction algorithm is shown in Figure 4 with the following steps:

Step 1: input the boundary voltage measurement $\mathbf{Z}$ and the uniform field conductivity distribution $\boldsymbol{\sigma}_0$.

Step 2: calculate the sensitivity matrix $\mathbf{S}_p$ and change in boundary voltage value $\Delta\mathbf{Z}_p$ using $\boldsymbol{\sigma}_p$, and then calculate the correction coefficient β_{p+1}.

Step 3: calculate the approximate increment of conductivity distribution $\Delta\boldsymbol{\sigma}_p$ after M iterations using the conventional Landweber iterate algorithm.

Step 4: correct $\Delta\boldsymbol{\sigma}_p$ using β_{p+1}.

Step 5: determine whether or not it is necessary to correct the sensitivity matrix. If necessary, return to Step 2. If not, output the conductivity distribution $\boldsymbol{\sigma}_{p+1}$.

4. Simulation and Results

4.1. Experimental Conditions. MatLab is used for simulation. The configuration of the simulated ERT sensor is listed below:

(i) Circular inner diameter: 50 mm

(ii) Liquid conductivity: 1 S/m

(iii) Gas conductivity: 0 S/m

(iv) Number of electrodes: 16

(v) Excitation and measurement mode: current injection to adjacent electrode pair and voltage measurement from the other adjacent electrode pairs (see Figure 1)

(vi) Number of independent measurement: 104

(vii) Number of finite elements: 1536 (see Figure 5)

To verify the proposed algorithm, three algorithms are used to reconstruct images for the four models, as shown in Figure 6. A uniform field is used as the initial distribution. The three algorithms are shown in Table 1.

In Algorithm 1 (uncorrected), the conventional Landweber iterative algorithm [10] is used and the sensitivity matrix is not corrected during the iterative process. In Algorithm 2 [12] ($\beta_{p+1} = 1$), $\beta_{p+1} = 1$. $M = 500$, when $p = 1$, and $M = 100$, when $p > 1$. $p = 0, 1, \ldots, P$, $P = 10$ and $\varepsilon = 0$. In Algorithm 3 ($\beta_{p+1} = 1.2 - (|\Delta Z_p|/|Z_p|)$), the algorithm proposed in this paper is used, $\beta_{p+1} = B - (|\Delta Z_p|/|Z_p|)$, $B = 1.2$. $M = 500$, when $p = 1$, and $M = 100$, when $p > 1$. $p = 0, 1 \ldots P$, $P = 10$ and $\varepsilon = 0$.

A reconstruction error and a correlation coefficient are used to evaluate the reconstruction results. The smaller the reconstruction error and the greater the reconstruction correlation means higher image quality [10]:

$$\text{Reconstruction error} = \frac{\|\widehat{\sigma} - \boldsymbol{\sigma}\|}{\|\boldsymbol{\sigma}\|} \times 100\%,$$

$$\text{Correlation coefficient} = \frac{\sum_{i=1}^{K}\left(\boldsymbol{\sigma}_i - \overline{\sigma}\right)\left(\widehat{\sigma}_i - \overline{\widehat{\sigma}}\right)}{\sqrt{\sum_{i=1}^{K}\left(\boldsymbol{\sigma}_i - \overline{\sigma}\right)^2 \sum_{i=1}^{K}\left(\boldsymbol{\sigma}_i - \overline{\widehat{\sigma}}\right)^2}}, \tag{17}$$

where $\widehat{\sigma}$ is the calculated conductivity distribution, $\boldsymbol{\sigma}$ is the true conductivity distribution, and $K = 1536$ is the number of elements in the sensing area.

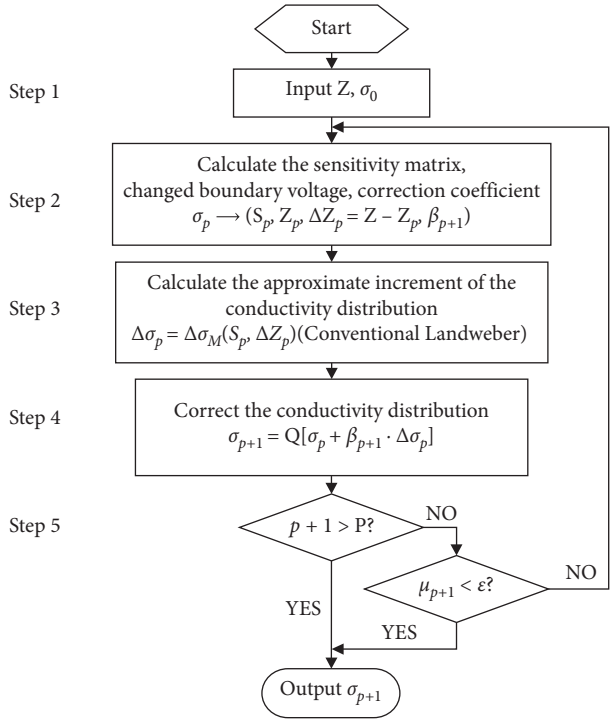

Figure 4: Block diagram of improved Landweber iterate algorithm.

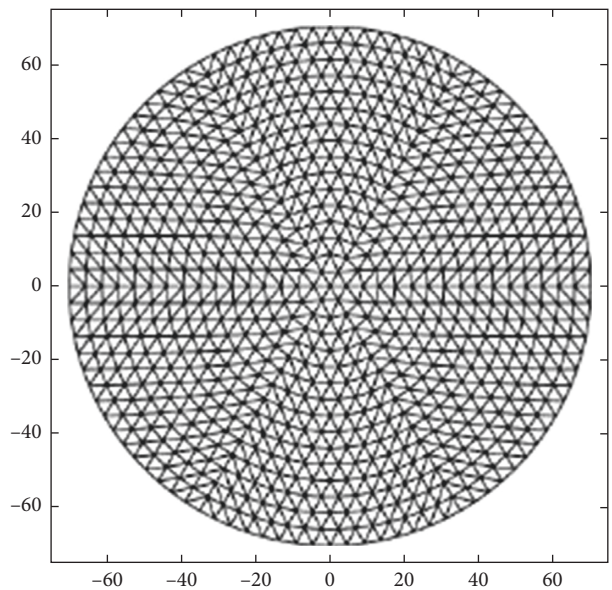

Figure 5: Mesh grid.

Quantitative analysis is performed by calculating the square sum of the substitution error of the matrix:

$$\text{Matrix substitution error} \left\|\boldsymbol{\eta}_p\right\| = \left\|\left(\mathbf{S}_p - \mathbf{S}\right) \cdot \boldsymbol{\sigma}\right\|. \quad (18)$$

4.2. Results and Analysis

4.2.1. Results with Noise Free Data. Without considering noise, the above three algorithms are used for reconstruction and the results are shown in Figure 7. With Algorithm 1, the reconstructed images with 500 iterations, 600 iterations, and 1400 iterations are given. For Algorithms 2 and 3, the reconstructed images after 1, 2, and 10 corrections are given, and the images correspond to iterations 500 times, 600 times, and 1400 times. The third column ($\beta_{p+1} = 1.2 - (|\Delta Z_p|/|Z_p|)$) is obtained using Algorithm 3.

In Figure 7, the first column is obtained by Algorithm 1, the second column by Algorithm 2, and the third column by Algorithm 3. As can be seen, after sensitivity matrix correction (2nd column and 3rd column), the artifacts of the reconstructed images are reduced and the boundary between two phases is clear. Comparing with Algorithm 2 (the 2nd column in Figure 7), Algorithm 3 reduces the artifacts of reconstruction images, where the contour of the discrete phase shrinks obviously and is close to the actual model distribution, as shown in Figure 6.

Quantitative analyses of the reconstructed images are showed in Figures 8 and 9. Note that the sensitivity matrix is not corrected in Algorithm 1, and the number of corrections represents the number of iterations corresponding to the other two algorithms.

From Figures 8 and 9, it can be seen that the quality of the images obtained by Algorithm 3 are obviously improved. For models D2 and D3, the differences between the model boundary voltage and the uniform field boundary voltage are relatively small (see Figure 10(a)) and the initial correction coefficient is larger (see Figure 10(b)). After the first time distribution correction, the distributions reconstructed by Algorithm 3 have larger image errors (as shown in Figures 8(b) and 8(c)) and lower correlations (as shown in Figures 9(b) and 9(c)), but the quality of reconstructed images obtained after the subsequent correction are improved, compared with Algorithms 1 and 2. For the models D1 and D4, the initial changes in voltage are greater (see Figure 10(a)). After punitive restraint on the reconstruction distribution, the reconstruction errors are decreased (as shown in Figures 8(a) and 8(d)) and reconstruction correlation coefficients are obviously increased (as shown in Figures 9(a) and 9(d)).

Quantitative analysis of matrix substitution error is shown in Figure 11. It can be seen that for the models D1, D3, and D4 that the square sum of the matrix substitution error $\|\boldsymbol{\eta}_p\|$ is significantly reduced after the sensitivity matrix is modified by the proposed algorithm. For the model D2, $\|\boldsymbol{\eta}_p\|$ increases after the first correction, the reason for this is the constant term $B = 1.2$, which makes the $\beta > 1$ (see Figure 10(b)), resulting in over relaxation. However, the error after the second correction is markedly reduced. The error in the subsequent correction process has also been in a downward trend. Compared with Algorithm 2 ($\beta_{p+1} = 1$) and Algorithm 3, if the initial matrix substitution error $\|\boldsymbol{\eta}_0\|$ is small (see Figures 11(b) and 11(c)), both algorithms can effectively reduce the matrix substitution error $\|\boldsymbol{\eta}_p\|$, and the effect of the penalty factor is not obvious. However, when the initial error $\|\boldsymbol{\eta}_0\|$ is large (see Figures 11(a) and 11(d)), the reduction of the error $\|\boldsymbol{\eta}_p\|$ after the correction of the sensitivity matrix is more obvious with Algorithm 3. It

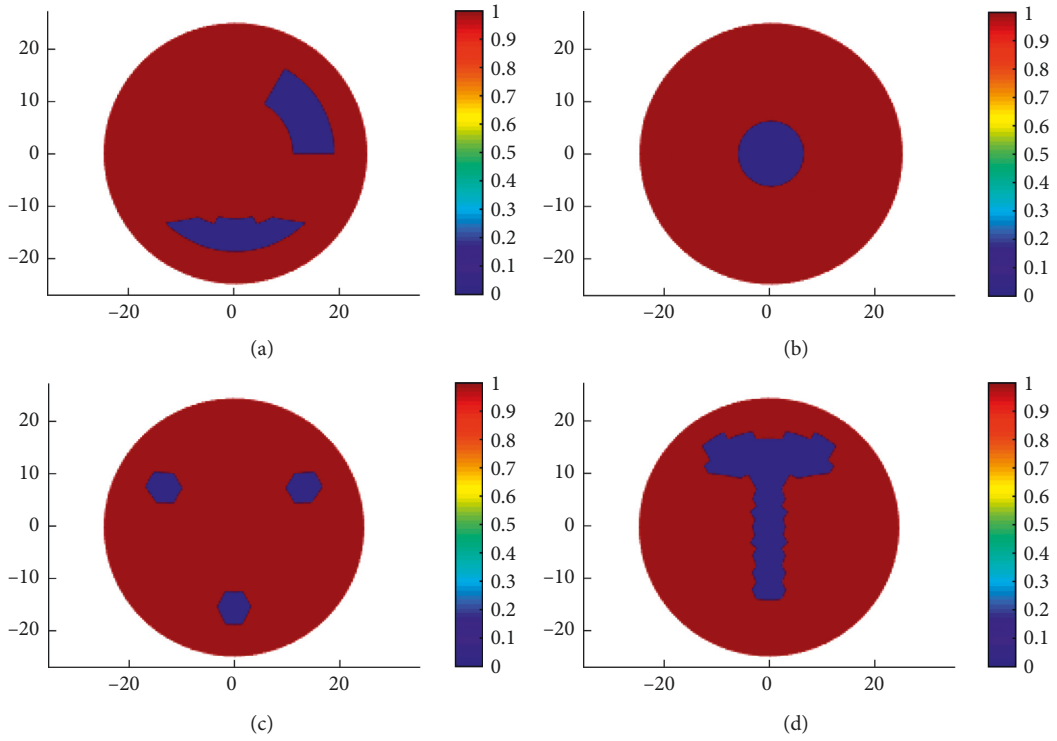

Figure 6: Four conductivity distribution models for simulation. (a) Model D1 (b) Model D2. (c) Model D3. (d) Model D4.

Table 1: Algorithm table.

Algorithm 1 [10, 16]	$\begin{cases} \Delta\boldsymbol{\sigma}_1 = \mathbf{S}^T \Delta\mathbf{Z} \\ \Delta\boldsymbol{\sigma}_{k+1} = \Delta\boldsymbol{\sigma}_k + \alpha \cdot \mathbf{S}^T (\Delta\mathbf{Z} - \mathbf{S} \cdot \Delta\boldsymbol{\sigma}_k) \\ \boldsymbol{\sigma} = Q[\boldsymbol{\sigma}_0 + \Delta\boldsymbol{\sigma}_M] \end{cases}$
Algorithm 2 [12]	$\begin{cases} \Delta\boldsymbol{\sigma}_p = \Delta\boldsymbol{\sigma}_M (S_P, \Delta Z_P) \text{(Conventional Landweber)} \\ \boldsymbol{\sigma}_{p+1} = Q[\boldsymbol{\sigma}_p + \beta_{p+1}\Delta\boldsymbol{\sigma}_p] \\ \beta_{p+1} = 1 \end{cases}$
Algorithm 3	$\begin{cases} \Delta\boldsymbol{\sigma}_p = \Delta\boldsymbol{\sigma}_M (S_P, \Delta Z_P) \text{(Conventional Landweber)} \\ \boldsymbol{\sigma}_{p+1} = Q[\boldsymbol{\sigma}_p + \beta_{p+1}\Delta\boldsymbol{\sigma}_p] \\ \beta_{p+1} = B - (\lvert\Delta\mathbf{Z}_p\rvert / \lvert\mathbf{Z}_p\rvert) \end{cases}$

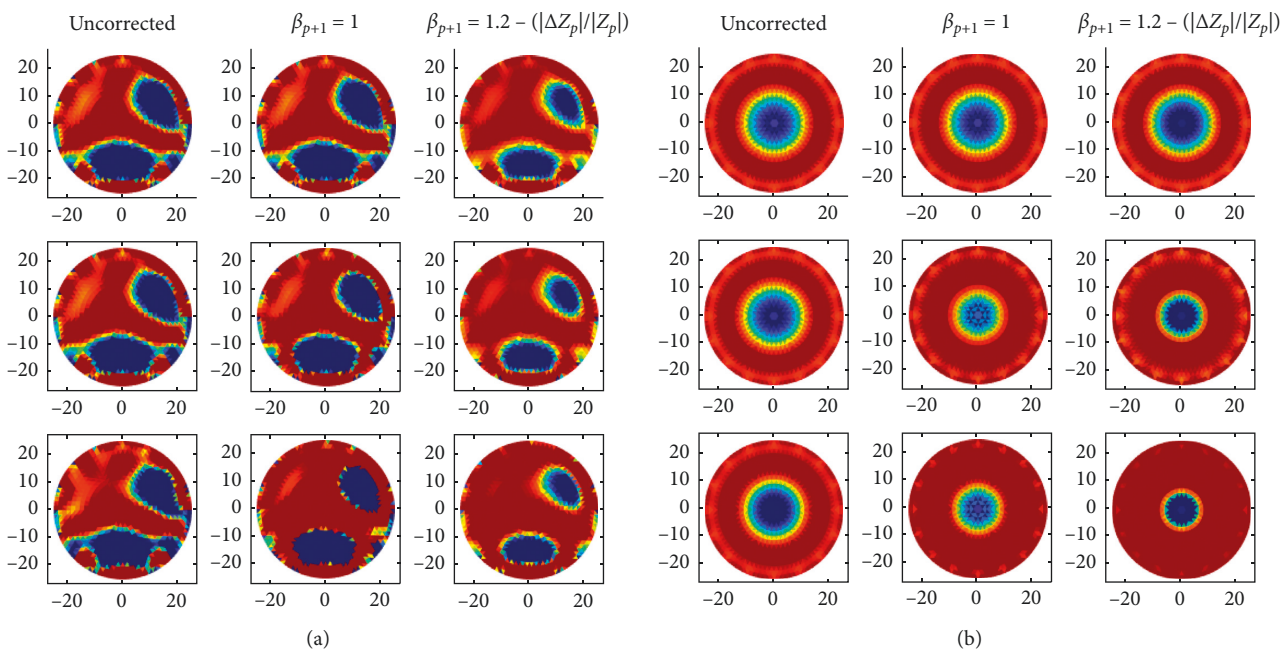

Figure 7: Continued.

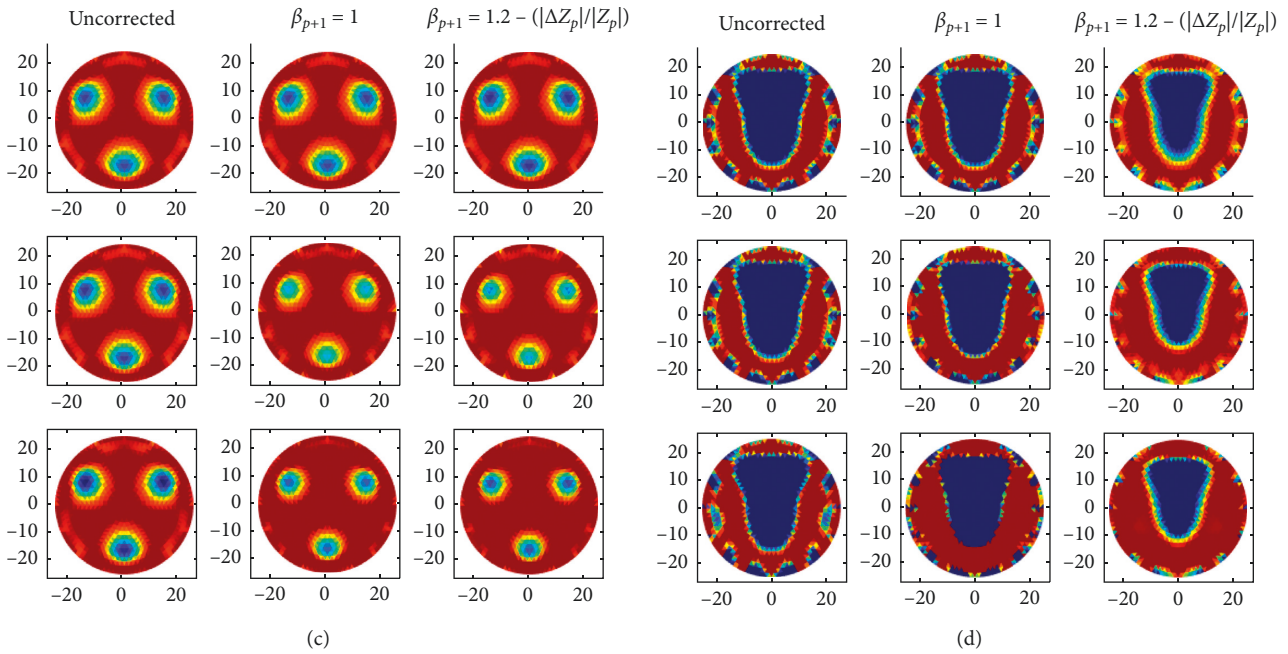

Figure 7: Reconstruction of three algorithms without noise. (a) Reconstructed image of model D1. (b) Reconstructed image of model D2. (c) Reconstructed image of model D3. (d) Reconstructed image of model D4.

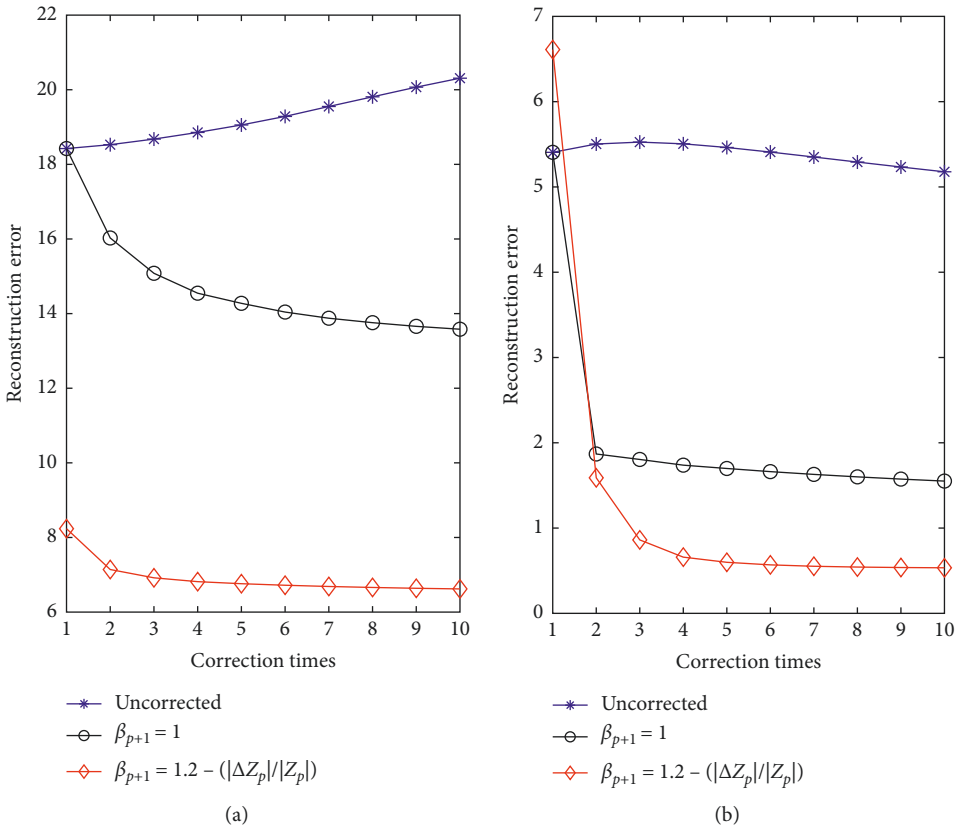

Figure 8: Continued.

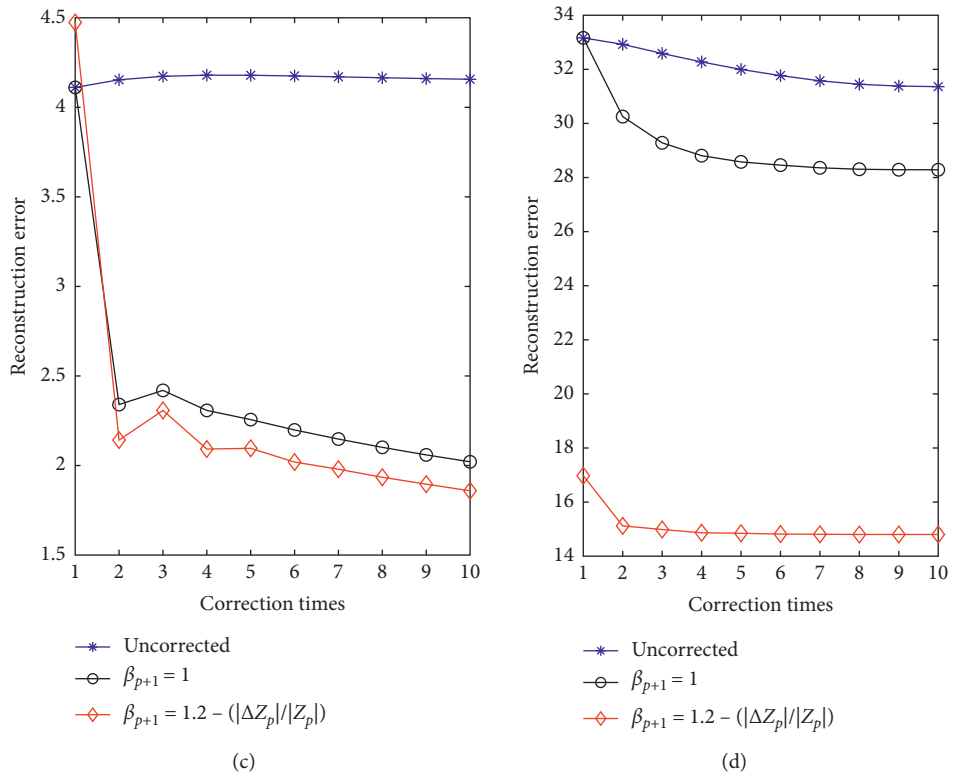

Figure 8: Reconstruction errors of three algorithms without noise. (a) D1. (b) D2. (c) D3. (d) D4.

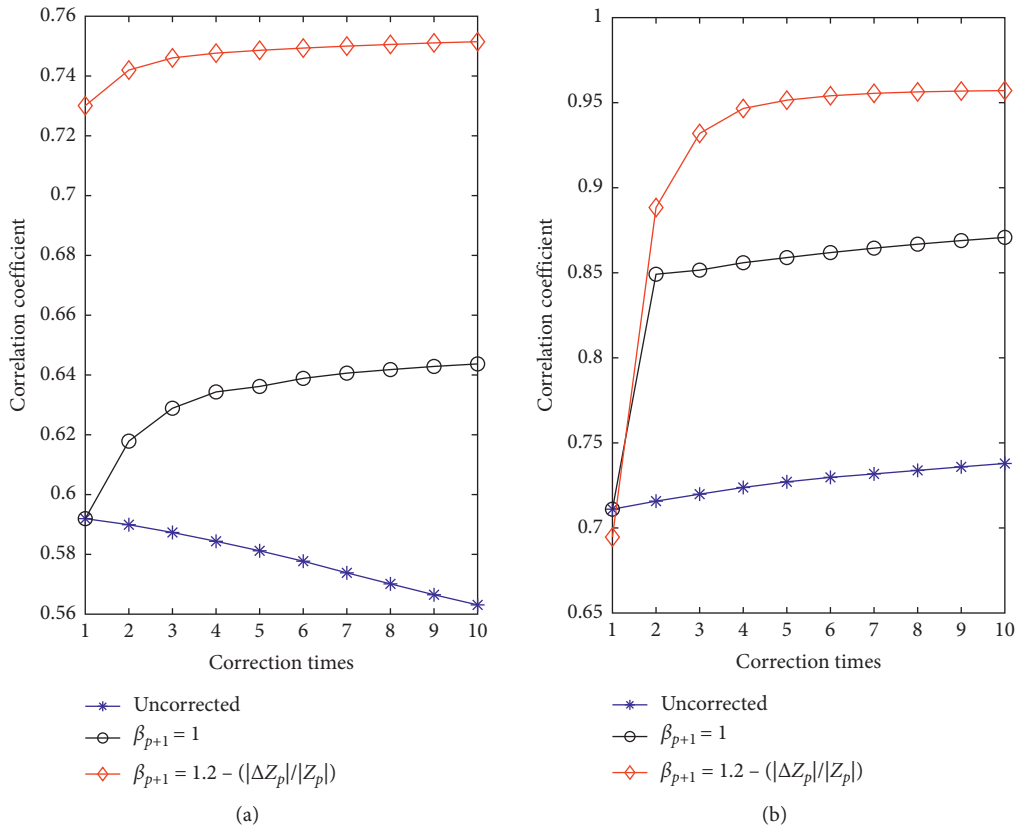

Figure 9: Continued.

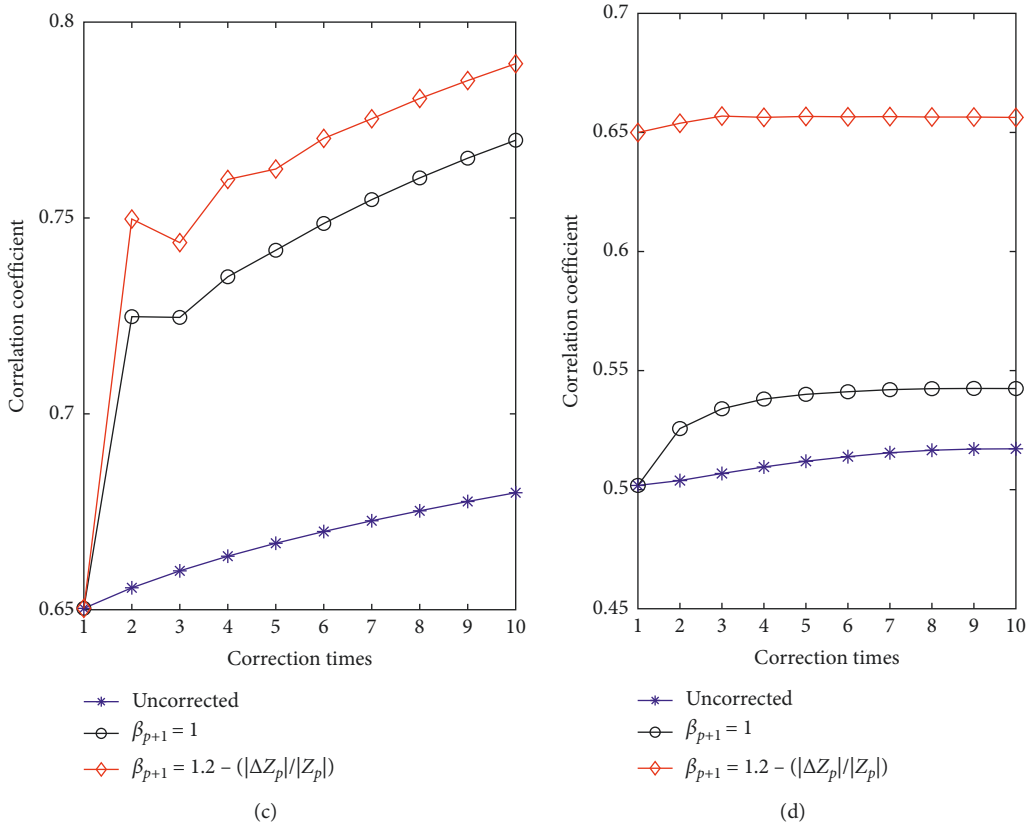

Figure 9: Correlation coefficients of three algorithms without noise. (a) D1. (b) D2. (c) D3. (d) D4.

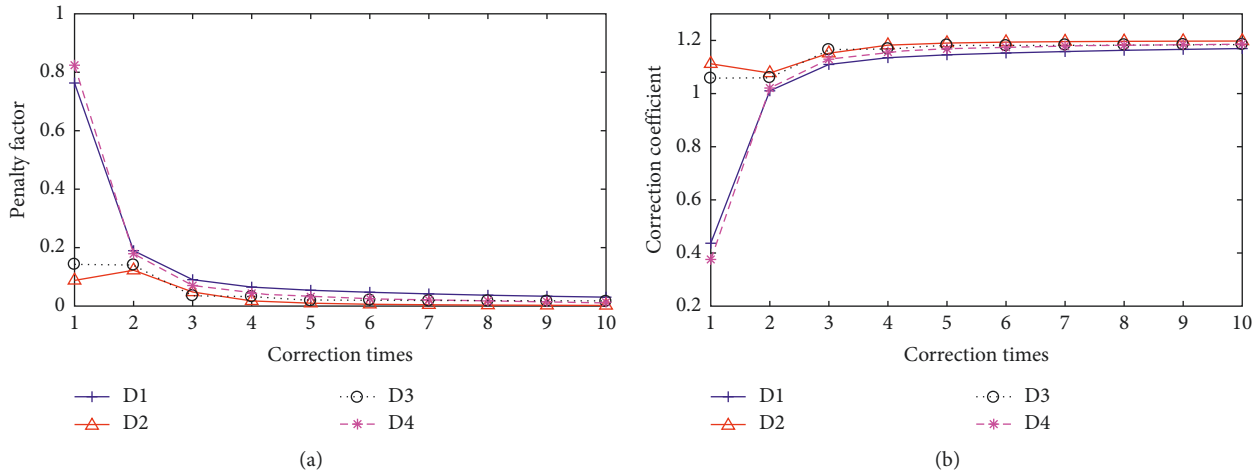

Figure 10: Penalty factors and correction coefficients of four models. (a) Penalty factors/relative changes in boundary voltage. (b) Correction Coefficients.

can also be seen from Figures 8 and 9 that for the models D1 and D4, the decrease in error and the improvement of the correlation coefficient is more significantly with Algorithm 3.

Because the correction requires additional calculation of the sensitivity matrix, the amount of computation increases significantly. Therefore, the number of matrix corrections must be limited. It can be seen in Figures 8 and 9 that after twice corrections, the quality of the reconstructed images has been greatly improved and the sensitivity matrix has only been recalculated once at this time. Therefore, the distribution after correcting twice can be used as the final result. Figure 12 shows data comparison with different algorithms in terms of the reconstruction error and correlation

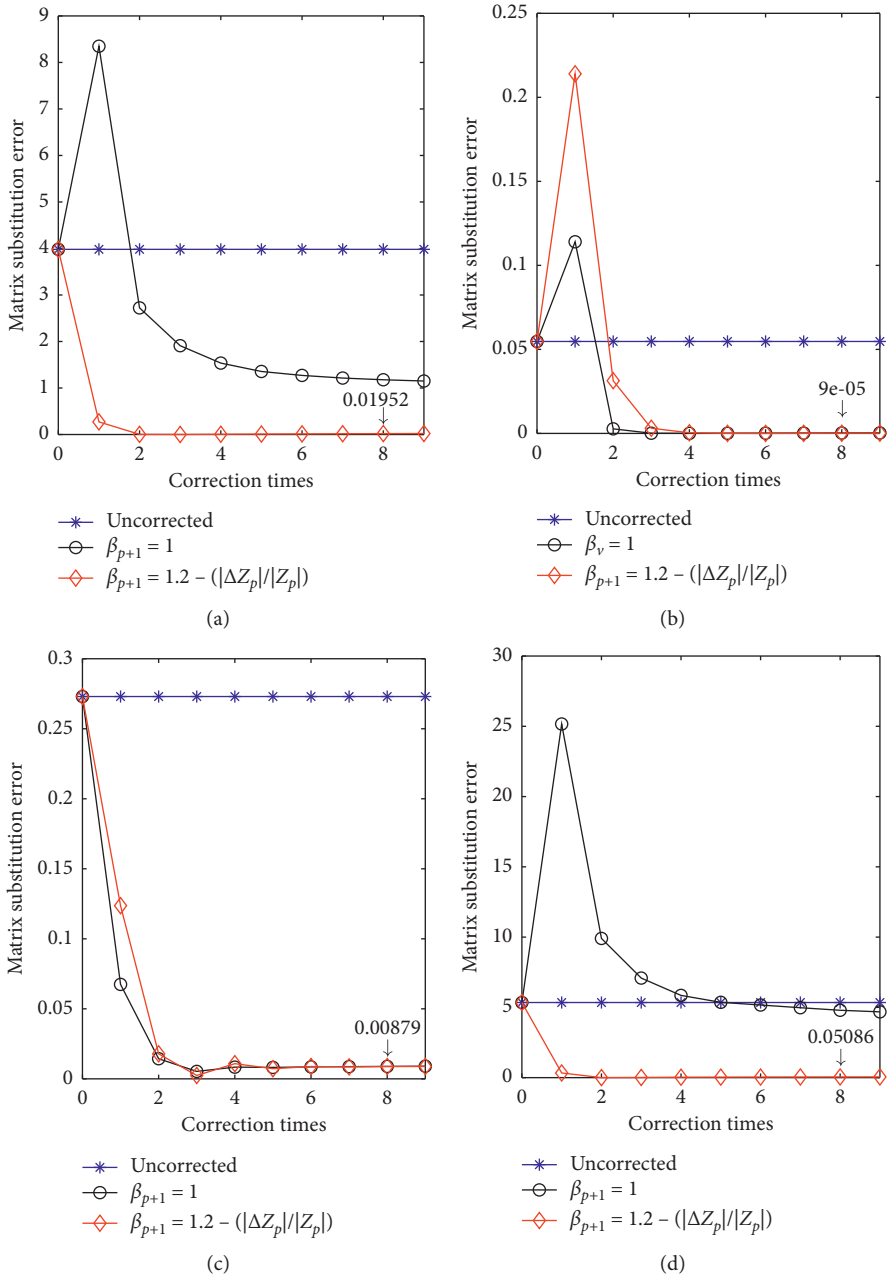

Figure 11: Matrix substitution error $\|\boldsymbol{\eta}_p\|$. (a) D1. (b) D2. (c) D3. (d) D4.

coefficient after corrected twice. It can be seen that errors are obviously reduced and correlations improved with Algorithm 3.

From the quantitative analyses, it can be found that the reconstruction errors are significantly reduced with the proposed algorithm and the correlations improved.

4.2.2. Results with Noisy Data. Because noise is inevitable and affects image reconstruction, it is necessary to analyse the antinoise ability of the algorithm. By adding random noise to the boundary voltage vector, the signal-to-noise ratio (SNR) becomes 30 dB. The three algorithms are used to perform 600 iterations for the four models. The obtained images are shown in Figure 13. With Algorithms 2 and 3, the sensitivity matrices are corrected once and reconstructed distributions are corrected twice.

It can be seen in Figure 13 that reconstructed images by Algorithm 3 are less distorted with fewer artifacts than those obtained by the other two algorithms. Quantitative analyses of the reconstructed images with noise data are showed in Figure 14. It can be seen that the errors of reconstructed distributions obtained by Algorithm 3 are lower (see Figure 14(a)) and correlation coefficients are greater (see Figure 14(b)).

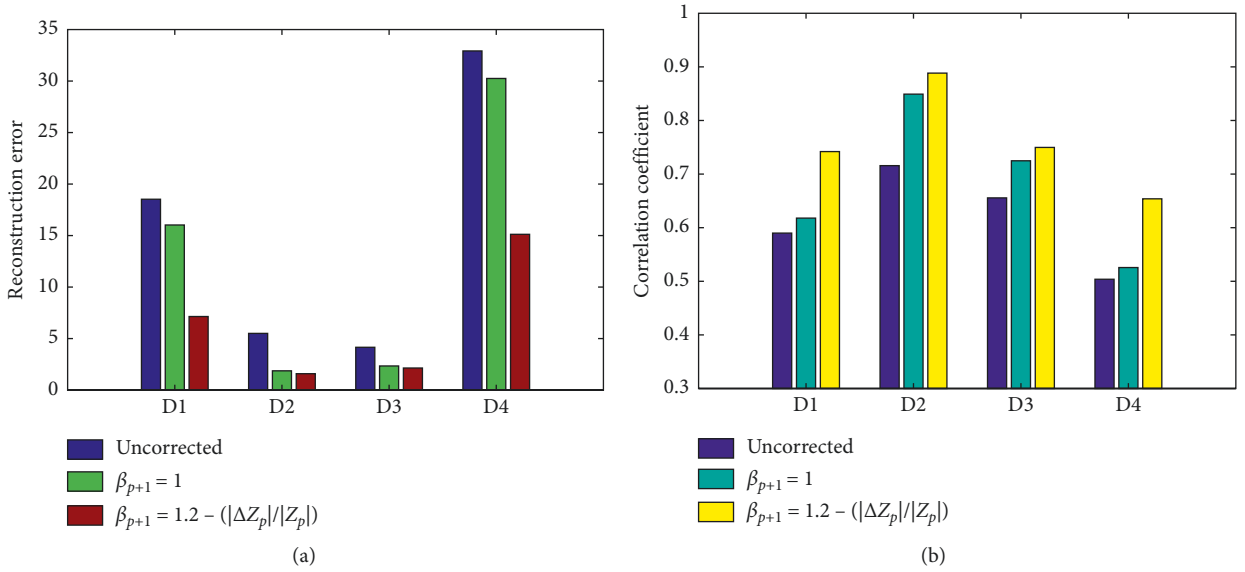

Figure 12: (a) Reconstruction errors and (b) image correlation coefficients with different algorithms after 600 iterations.

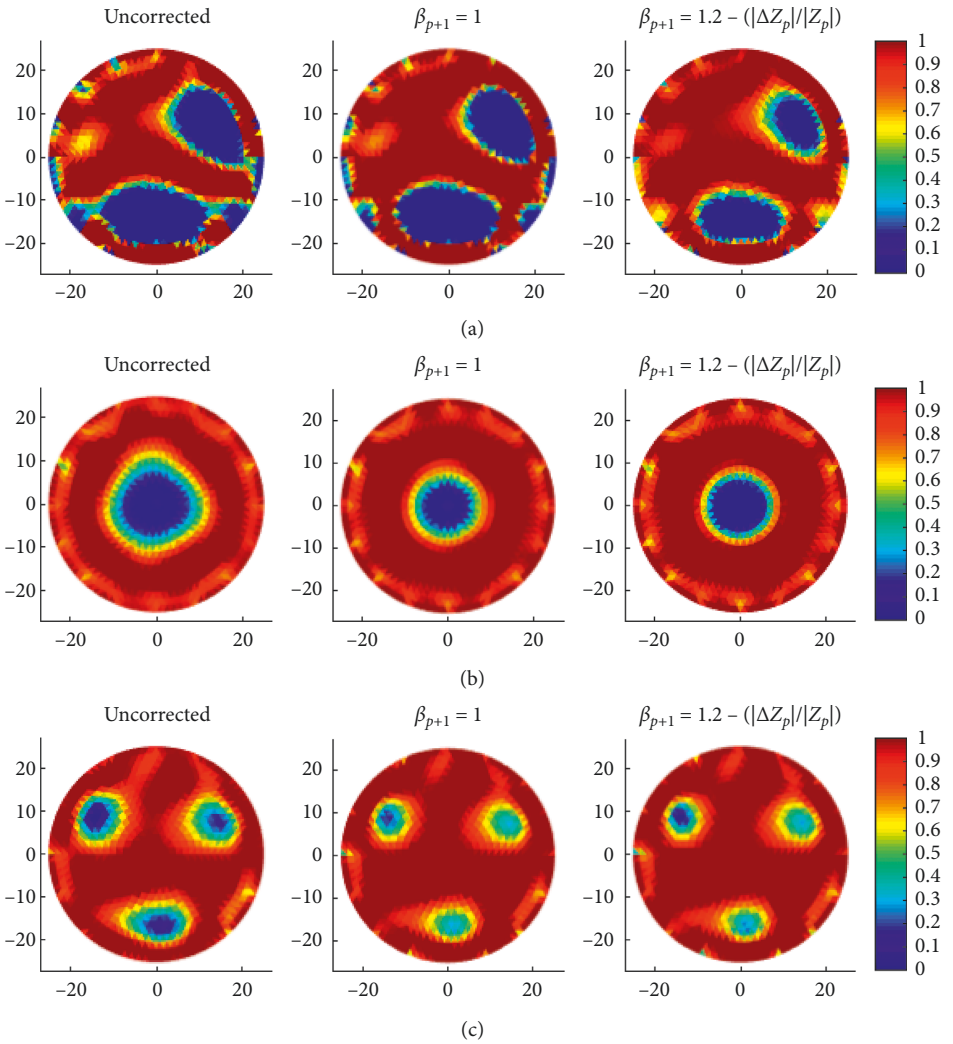

Figure 13: Continued.

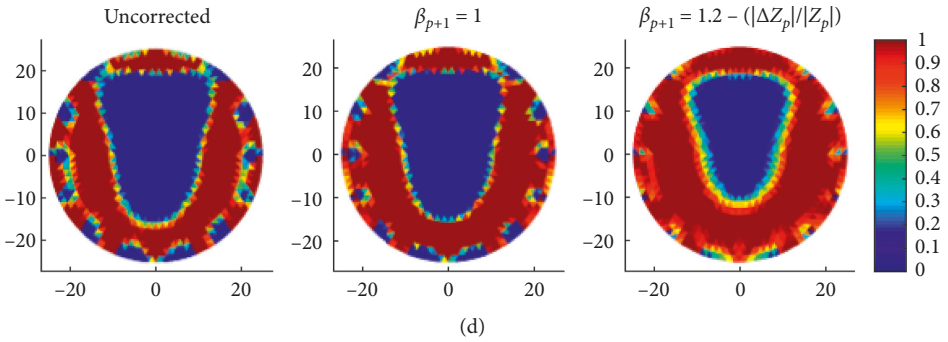

Figure 13: Reconstructed images after 600 iterations with noise. (a) Reconstructed images of D1. (b) Reconstructed images of D2. (c) Reconstructed images of D3. (d) Reconstructed images of D4.

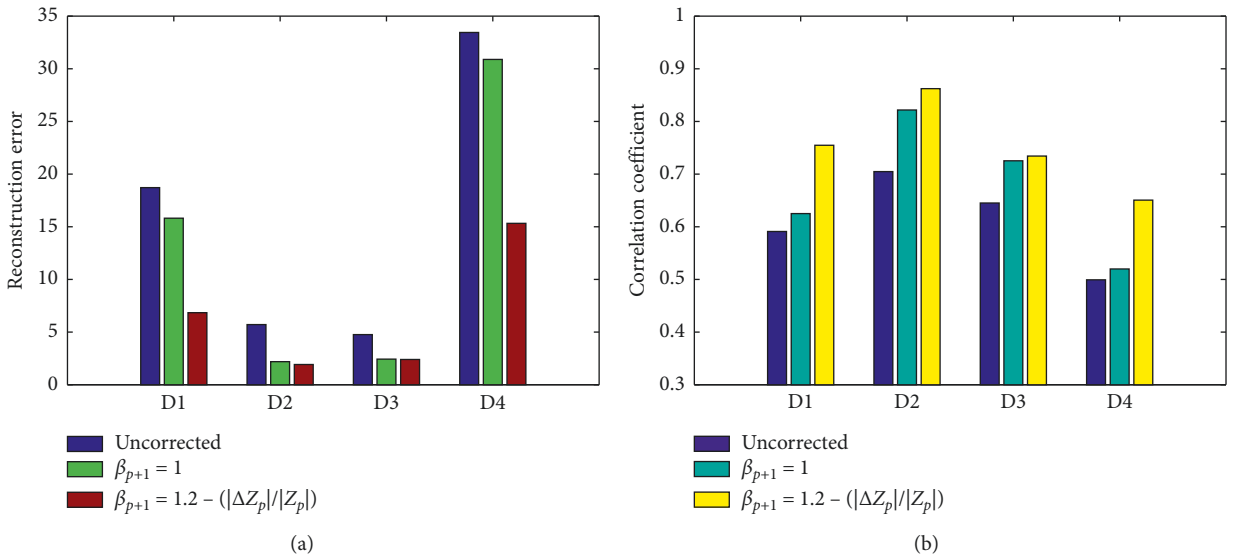

Figure 14: (a) Reconstruction errors and (b) image correlation coefficients of different algorithms after 600 iterations with noise.

From the above results, it is concluded that the reconstruction error can be effectively reduced and the correlation can be improved by the proposed algorithm.

4.2.3. Experimental Results. Experiment was conducted to validate the proposed algorithm. The experimental setup is shown in Figure 15, which was developed at the University of Leeds. Configurations of the experimental system are listed below.

(i) Injected current: 15.10 mA

(ii) Current Frequency: 9600 Hz

(iii) Diameter of test filed: 50 mm

(iv) ERT sensor: single plane 16-electrodes.

Six distribution models are selected, as shown in Figure 16. The three algorithms are used to reconstruct six models. The reconstructed images after 600 iterations with real data are shown in Figure 17.

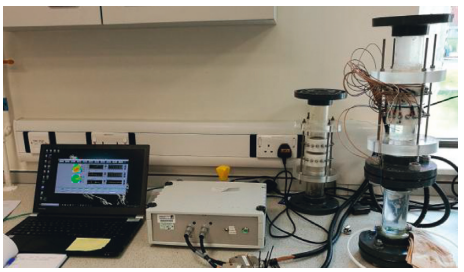

Figure 15: Experimental setup of the ERT test system.

It can be seen from Figure 17 that the proposed algorithm effectively distinguishes targets. For both models, the artifacts with the proposed algorithm are

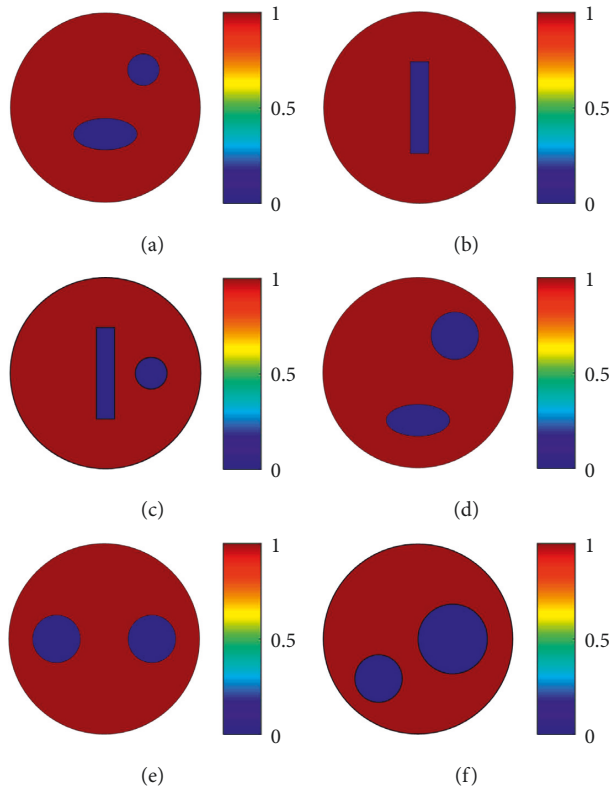

Figure 16: Conductivity distribution models for experimentation. (a) Model 1. (b) Model 2. (c) Model 3. (d) Model 4. (e) Model 5. (f) Model 6.

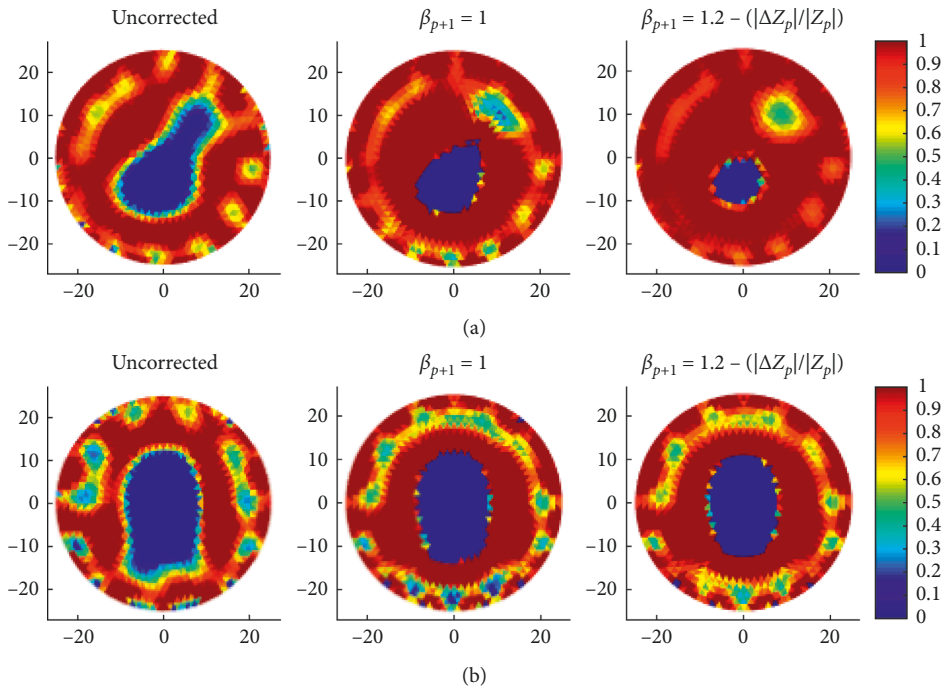

Figure 17: Continued.

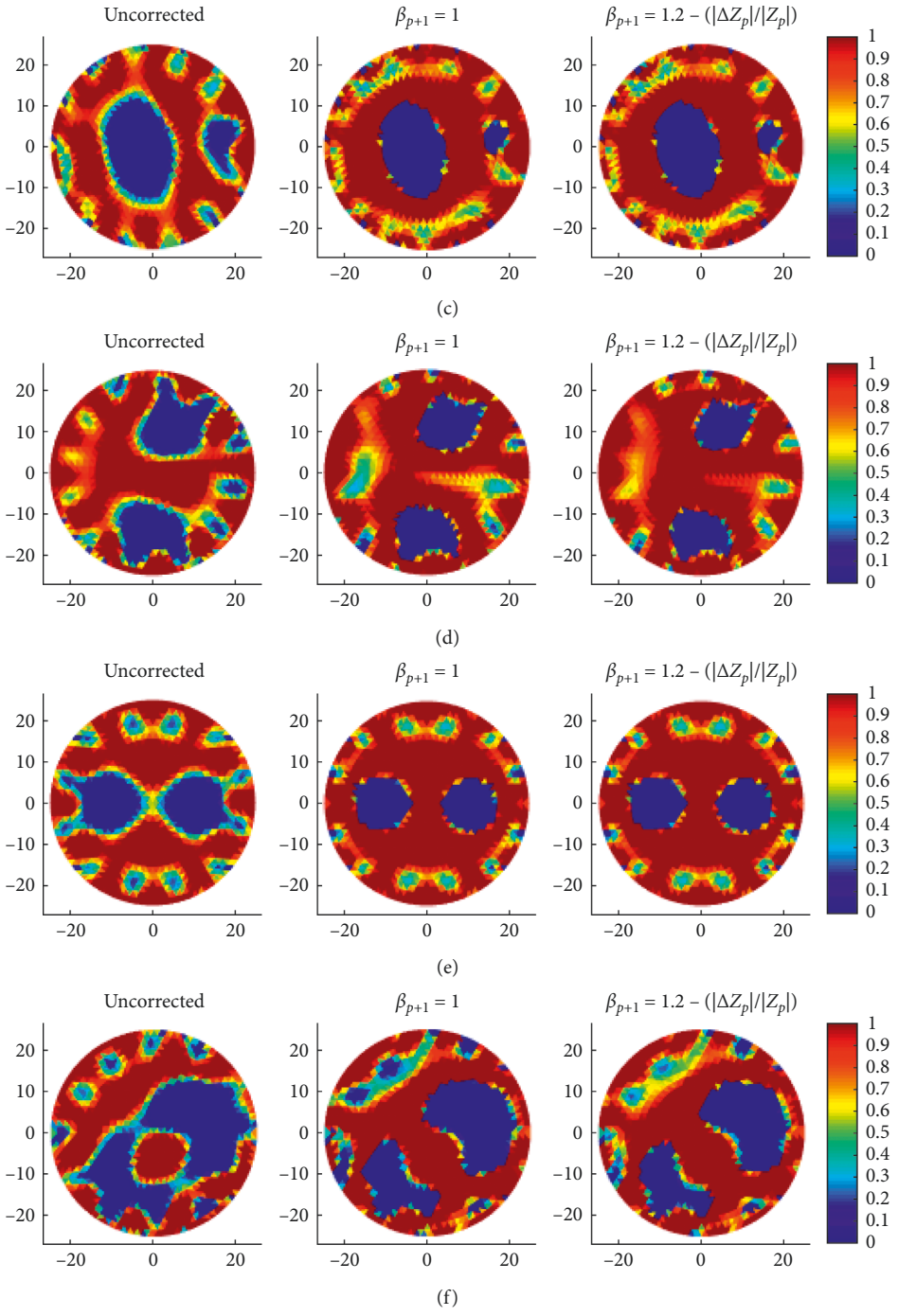

Figure 17: Reconstructed images after 600 iterations with real data. (a) Reconstructed images of Model 1. (b) Reconstructed images of Model 2. (c) Reconstructed images of Model 3. (d) Reconstructed images of Model 4. (e) Reconstructed images of Model 5. (f) Reconstructed images of Model 6.

less and the two-phase boundary of the distribution is clear.

5. Conclusions

In this paper, an image reconstruction algorithm for ERT is proposed. It is based on correction of the sensitivity matrix and Landweber iteration. The error introduced by the initial sensitivity matrix is estimated using the relative variation in the boundary voltage. According to the estimated value, the correction coefficient with a penalty factor is obtained and the distribution reconstructed from Landweber iteration and the initial sensitivity matrix are corrected. To improve the reconstruction accuracy, the distribution and sensitivity matrix are alternatively corrected.

Both simulation and experimental results show that the boundary between two phases of the distribution can be reconstructed by the proposed algorithm clearly. The artifacts are less and the distribution is more accurate than the traditional Landweber algorithm and the algorithm without the penalty factor. Quantitative analysis shows that the proposed algorithm is effective in reducing errors in particular when the initial error is large.

The correlation between the variation in the boundary voltage and the matrix substitution error is analyzed. In the future, research will be carried out on correlation to further reduce the image error and improve the reconstruction accuracy.

Data Availability

The data used in this paper to support the findings of this study are included in the article.

Conflicts of Interest

The authors declare that they have no conflicts of interest.

References

[1] F. Dickin and M. Wang, "Electrical resistance tomography for process applications," *Measurement Science and Technology*, vol. 7, no. 3, pp. 247–260, 1996.

[2] R. Babaei, B. Bonakdarpour, and F. Ein-Mozaffari, "The use of electrical resistance tomography for the characterization of gas holdup inside a bubble column bioreactor containing activated sludge," *Chemical Engineering Journal*, vol. 268, no. 3, pp. 260–269, 2015.

[3] A. Cultrera and L. Callegaro, "Electrical resistance tomography of conductive thin films," *IEEE Transactions on Instrumentation and Measurement*, vol. 65, no. 9, pp. 2101–2107, 2016.

[4] M. A. Díaz De Rienzo, R. Hou, and P. J. Martin, "Use of electrical resistance tomography (ERT) for the detection of biofilm disruption mediated by biosurfactants," *Food and Bioproducts Processing*, vol. 110, no. 1–5, 2018.

[5] Z. Shao, D. Wang, Y. Wang, X. Zhong, X. Tang, and D. Xi, "Electrical resistivity of coal-bearing rocks under high temperature and the detection of coal fires using electrical resistance tomography," *Geophysical Journal International*, vol. 204, no. 2, pp. 1316–1331, 2016.

[6] K. Li, Q. Wang, M. Wang, and Y. Han, "Imaging of a distinctive large bubble in gas-water flow based on size projection algorithm," *Measurement Science and Technology*, vol. 30, no. 9, In press, 2019.

[7] D. B. Geselowitz, "An application of electrocardiographic lead theory to impedance plethysmography," *IEEE Transactions on Biomedical Engineering*, vol. BME-18, no. 1, pp. 38–41, 1971.

[8] H. X. Wang and Z. Cao, "Nonlinearity of "soft" field in electrical impedance tomography system—based on statistical methods," *Journal of Tianjin University*, vol. 39, no. 5, pp. 543–547, 2006.

[9] C. G. Xie, S. M. Huang, M. S. Beck et al., "Electrical capacitance tomography for flow imaging: system model for development of image reconstruction algorithms and design of primary sensors," *IEE Proceedings G Circuits, Devices and Systems*, vol. 139, no. 1, pp. 89–98, 1992.

[10] W. Q. Yang, D. M. Spink, T. A. York, and H. McCann, "An image-reconstruction algorithm based on Landweber's iteration method for electrical-capacitance tomography," *Measurement Science and Technology*, vol. 10, no. 11, pp. 1065–1069, 1999.

[11] L. Peng, H. Merkus, and B. Scarlett, "Using regularization methods for image reconstruction of electrical capacitance tomography," *Particle & Particle Systems Characterization*, vol. 17, no. 3, pp. 96–104, 2000.

[12] L. Zhang, "A modified landweber iteration algorithm using updated sensitivity matrix for electrical impedance tomography," *International Journal of Advanced Pervasive and Ubiquitous Computing*, vol. 5, no. 1, pp. 17–29, 2013.

[13] L. Q. Xiao, H. X. Wang, and X. J. Xu, "Improved Newton-Raphson algorithm for electrical resistance tomography image reconstruction," *Proceedings of the Chinese Society of Electrical and Electronics Engineers*, vol. 32, no. 8, pp. 91–97, 2012.

[14] J. Lehr, "A vector derivation useful in impedance plethysmographic field calculations," *IEEE Transactions on Biomedical Engineering*, vol. 8, no. 4A, pp. 156-157, 1972.

[15] C. J. Kotre, "A sensitivity coefficient method for the reconstruction of electrical impedance tomograms," *Clinical Physics and Physiological Measurement*, vol. 10, no. 3, pp. 275–281, 1989.

[16] W. Q. Yang and L. Peng, "Image reconstruction algorithms for electrical capacitance tomography," *Measurement Science and Technology*, vol. 14, no. 1, pp. R1–R13, 2003.

[17] W. R. Breckon and M. K. Pidcock, "Mathematical aspects of impedance imaging," *Clinical Physics and Physiological Measurement*, vol. 8, no. 4A, pp. 77–84, 1987.